Volume 11
Number 10
21 May 2024
Pages 2283–2530

Materials Horizons

rsc.li/materials-horizons

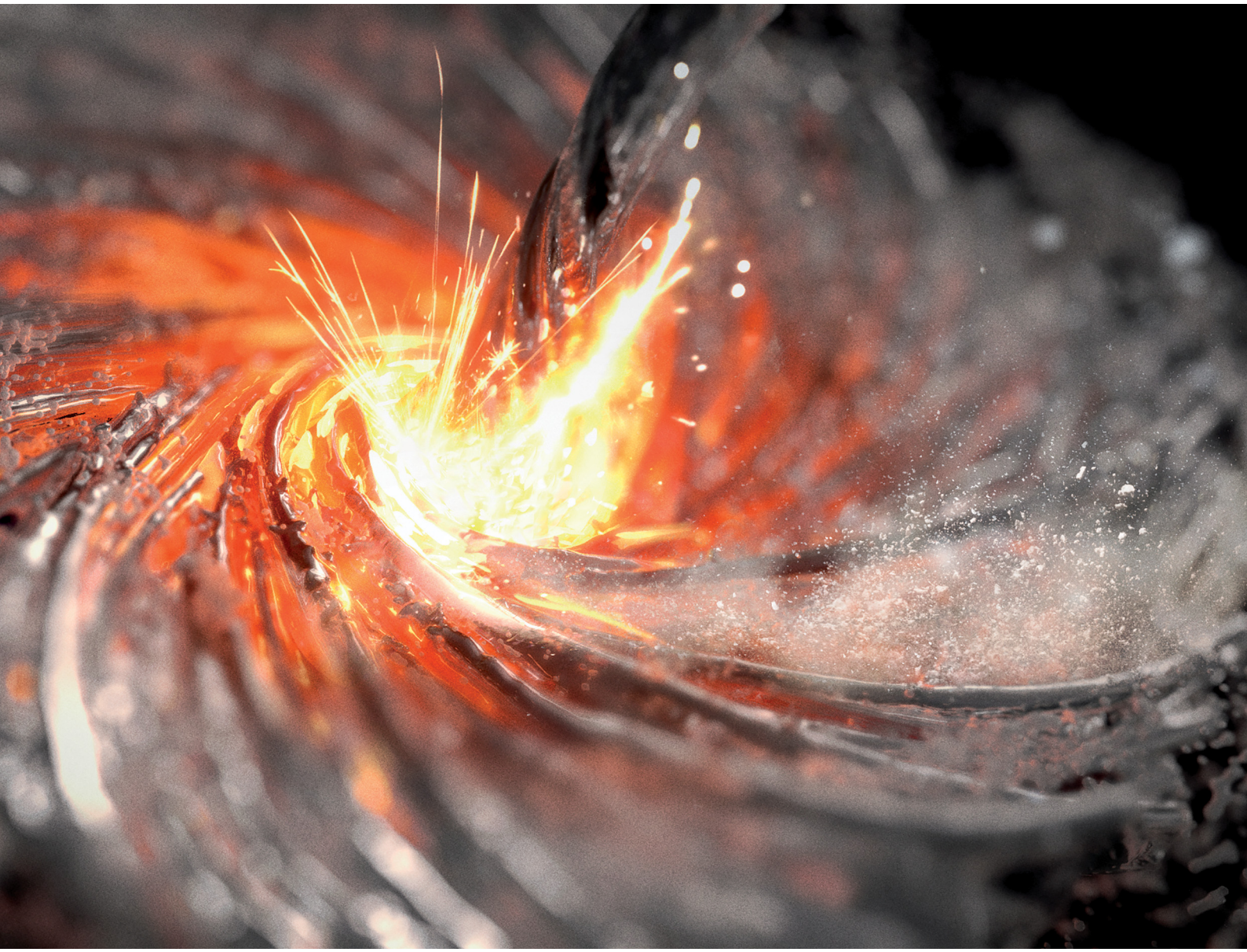

ISSN 2051-6347

ROYAL SOCIETY OF CHEMISTRY

COMMUNICATION
Alfred Amon, Emily E. Moore *et al.*
Aluminothermic reduction of CeO_2: mechanism of an economical route to aluminum–cerium alloys

10 YEARS ANNIVERSARY

Materials Horizons

ROYAL SOCIETY OF CHEMISTRY

COMMUNICATION

View Article Online
View Journal | View Issue

Cite this: *Mater. Horiz.*, 2024, 11, 2382

Received 24th January 2024,
Accepted 19th March 2024

DOI: 10.1039/d4mh00087k

rsc.li/materials-horizons

Aluminothermic reduction of CeO_2: mechanism of an economical route to aluminum–cerium alloys†

Alfred Amon, *[a] Emily E. Moore, *[a] Hunter B. Henderson,[a] Jibril Shittu,[a] Martin Kunz,[b] Shane Kastamo,[c] Nikolai Huotari,[c] Adam Loukus,[c] Ryan Ott,[d] David Weiss[c] and Scott K. McCall[a]

Cerium oxide is a low-value byproduct of rare-earth mining yet constitutes the largest fraction of the rare earth elements. The reduction of cerium oxide by liquid aluminum is proposed as an energy- and cost-efficient route to produce high-strength Al–Ce alloys. This work investigated the mechanism of a multi-step reduction reaction to facilitate the industrial adaptation of the process. Differential scanning calorimetry in combination with time-resolved synchrotron diffraction data uncovered the rate-limiting reaction step as the origin of the reported temperature dependence of reduction efficiency. This is the first *in situ* study of a metallothermic reaction mechanism and will serve as guidance for cost- and energy efficient industrial process control.

New concepts

Aluminothermic reduction of cerium oxide can significantly reduce the cost and energy-consumption associated with Al–Ce alloy production compared to conventional processes. The direct use of cerium compounds accrued during rare earth element (REE) mining makes light-weight REE a value-added co-product instead of a waste product. In this study we demonstrate a novel approach to produce Al–Ce alloys by reducing CeO_2 in liquid aluminum at 95% reduction efficiency. This work provides the first ever mechanistic insight into the reaction kinetics and intermediate products of an aluminothermic reaction, which reveal a multi-step reaction mechanism with complex temperature dependency, details that are necessary for scaling on an industrial level. This work provides the basis of an economic route to produce high strength Al–Ce alloys with enhanced dispersion strengthening from embedded Al_2O_3 particles.

Nearly 200 years ago, H. C. Oersted revolutionized metallurgy, as he prepared metallic aluminum through the reduction of $AlCl_3$ by potassium amalgam, inventing the metallothermic reaction.[1] Since then, many elements have been isolated for the first time by reaction of their compounds with a more reactive metal to form a more stable compound and the sought-after elemental metal.[2] Metallothermic reactions remain a crucial technology applied in the iron thermite reaction for welding of train tracks and the industrial production of metals such as Be, Ti, Ta and the rare earth elements through the reduction of their halides by Mg, Na or Ca.[3,4]

Rare earth elements tend to be co-located in ore deposits and are treated together in extraction. Cerium is the majority element in most deposits, and the growing need for Nd, Pr and the heavy lanthanides in permanent magnets and other energy transition technologies results in costly stockpiling of cerium oxide that has low demand.[5–7] Aluminum alloys with up to 10 wt% cerium have been developed in the last decade as a new class of light-weight, high-temperature materials, exploiting formation of the high-melting intermetallic compound Ce_3Al_{11} in the microstructure.[6,8,9] As such, Al–Ce alloys are a competitive high strength alloy class that creates a high-value demand for excess cerium to help stabilize the rare earth market.[10,11]

Al–Ce alloys are produced by alloying Al melts with metallic Ce, which itself is produced by calciothermic reduction of $CeCl_3$ in a prior energy-intensive step. This step can potentially be avoided by leveraging the following reaction (1), with a standard reaction enthalpy of -30.1 kJ mol^{-1}.

$$CeO_2 + \frac{4}{3}Al \rightarrow Ce + \frac{2}{3}Al_2O_3 - 30.1\ \text{kJ mol}^{-1} \quad (1)$$

The direct reduction of CeO_2 in liquid aluminum shows promise as an economical route to produce Al–Ce alloys, circumventing the production of Ce metal, which will reduce the environmental footprint and facilitate commercial adaptation.

Mechanistic understanding of metallothermic reactions supports the effective parameter optimization in industry but is still in its infancy due to the harsh reaction conditions of

[a] *Lawrence Livermore National Laboratory, 7000 East Ave, Livermore, CA 94550, USA. E-mail: amon1@llnl.gov, moore255@llnl.gov*
[b] *Lawrence Berkeley National Laboratory, 1 Cyclotron Rd, Berkeley, CA 94720, USA*
[c] *Loukus Technologies Inc., 58390 Centennial Number 6 Road, Calumet, MI 49913, USA*
[d] *Ames National Laboratory, 2415 Pammel Dr, Ames, IA, 50011, USA*

† Electronic supplementary information (ESI) available. Experimental methods as well as details on diffraction experiments, metallography, and DSC. The authors cite additional ref. 32–46. See DOI: https://doi.org/10.1039/d4mh00087k

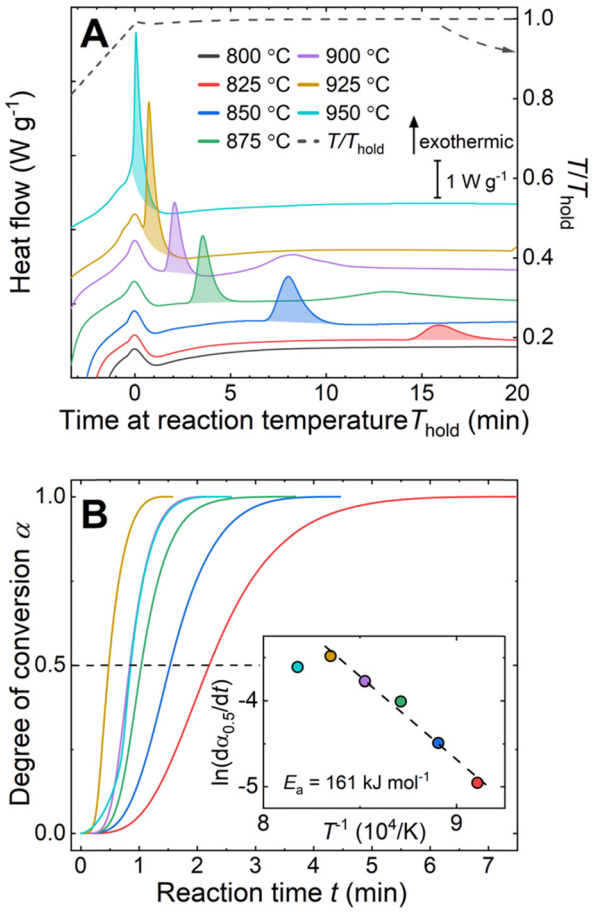

Fig. 1 Calorimetry of Al–CeO_2 mixtures with color legend in the top panel. (A) Detailed view of isothermal holds where the shaded areas reflect the heat of reaction. Curves are offset for clarity. (B) Corresponding kinetic curves of degree of conversion *vs.* reaction time for aluminothermic reduction reactions, derived from peak integration in (A). Inset to (B): Arrhenius-plot with fit (dashed line) to the data from 825 °C to 925 °C provides E_a.

these highly exothermic reactions. Aluminothermic reactions with ZrO_2,[12] MoO_3,[13,14] $NaVO_3$,[15] MgO,[16] and Cr_2O_3,[17] have been studied for industrial alloy production, while reduction of ZnO,[18,19] was investigated by preparing Al/Al_2O_3 matrix composites.

Early investigations of the aluminothermic reduction of CeO_2,[20] and cerium carbonate,[21] reported a strong temperature dependence of the conversion efficiency. No study has reported data on intermediate reaction products or mechanistic details.

To further fundamental understanding and accelerate industrial adaptation, we have investigated the reaction kinetics and mechanism of the aluminothermic reduction of CeO_2 for the preparation of Al–Ce alloys, by means of differential scanning calorimetry (DSC), metallography, time-resolved synchrotron X-ray diffraction, and thermodynamic calculations.

The reaction between liquid aluminum and CeO_2 particles was investigated *via* isothermal holds (800 °C $\leq T_{hold} \leq$ 950 °C) in DSC on pressed pellets of aluminum–CeO_2 powder mixtures (Fig. 1A, experimental details in ESI†). The onset time of the exotherms (shaded areas under curves in Fig. 1A) was reduced with increasing reaction temperature from 15 min to less than 1 minute for the reactions at 825 °C and 950 °C, respectively.

The kinetics of the reaction were further examined using the isothermal kinetic curves, *i.e.* normalized integral curves of the integrated peak areas, as the integral curves were found less sensitive to uncertainties in reaction onset time and baseline.[22,23] The kinetic curves (Fig. 1B) revealed an accelerated reaction rate with increasing temperature up to 925 °C, while the rate at 950 °C did not increase further. The reaction rate $\frac{d\alpha}{dt}$ determined at half conversion (α = 0.5) confirmed the increase of the reaction rate with temperature and, using Friedman's isoconversional formulation of the Arrhenius equation (inset to Fig. 1B),[22,24,25] allowed estimation of an effective activation energy E_a = 161 kJ mol^{-1}. A second broad exothermic effect was observed with onset about 20, 13, 4 and 2 minutes after the completion of the initial reaction at 825, 850 °C, 875 °C and 900 °C, respectively (see Fig. 1A and Fig. S1, ESI†). This process of unclear origin appeared accelerated at higher temperatures.

The reaction products after the DSC measurement at 850 °C were identified by powder X-ray diffraction (PXRD, see Fig. S2, ESI†) as Al (Cu structure, $Fm\bar{3}m$, a(300 K) = 4.045(2) Å), CeO_{2-x} ‡ (CaF_2 structure, $Fm\bar{3}m$, a(300 K) = 5.4054(2) Å), Al_2O_3 (Corundum structure, $R\bar{3}c$, a(300 K) = 4.753(3) Å, c(300 K) = 12.984(4) Å) and Ce_3Al_{11} (La_3Al_{11} structure, $Immm$, a(300 K) = 4.3879(2) Å, b(300 K) = 10.0513(6) Å, c(300 K) = 13.0079(7) Å) confirming successful reduction of $Ce^{IV}O_{2-x}$ to $Ce^0_3Al_{11}$ (arguendo, we assume oxidation state Ce^0 in the intermetallic compounds). After reaction at 950 °C, Al, Al_2O_3 and Ce_3Al_{11} but no residual CeO_{2-x} were observed, and the relative amounts of Ce_3Al_{11} and Al_2O_3 doubled and tripled, respectively, compared to the reaction at 850 °C (see Fig. S3 and Table S1 for details, ESI†).

Scanning electron micrographs of the pellet after reaction at 950 °C (Fig. 2) showed large agglomerates of Ce_3Al_{11} grains with 30 μm to 50 μm diameter in an aluminum matrix, as identified by energy-dispersive X-ray spectroscopy (EDS) (Table S2 and Fig. S4, ESI†). Higher magnification revealed small crystallites of Al_2O_3 with a narrow size distribution around 5 μm embedded in the Ce_3Al_{11} and Al phases (red arrows in Fig. 2B–E). These are significantly larger than the Al_2O_3 particles with 200 nm diameter observed in composite materials produced by reduction of $Ce_2(CO_3)_3$.[21]

After reaction at 850 °C, the micrographs (Fig. S5, ESI†) showed significant amounts of unreacted CeO_{2-x} particles as well as Al and Ce_3Al_{11} grains. Detailed investigation of the micrographs (Fig. S5B–E, ESI†) revealed that the Ce_3Al_{11} grains appear to crystallize only from within the aluminum matrix.

To better understand the kinetics and mechanism of the aluminothermic reduction of CeO_2 as well as the origin of the observed second exotherm in DSC, time-resolved synchrotron diffraction data were recorded on pressed pellets of aluminum–CeO_2 powder mixtures contained in glass capillaries (12.2.2, Advanced Light Source/LBNL, USA). Diffraction data were recorded while ramping the sample temperature to the isothermal hold temperature (T_{hold} = 850 °C, 900 °C and 950 °C) to

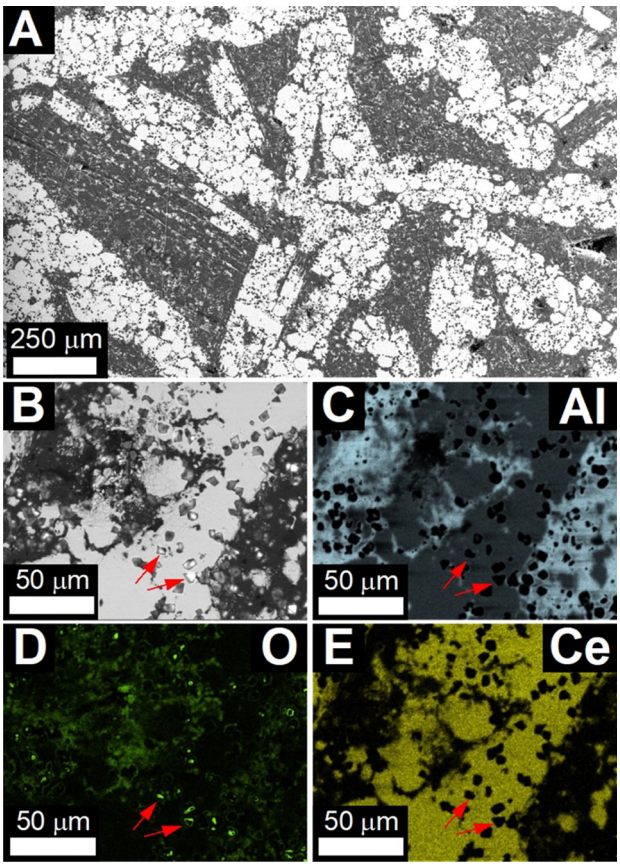

Fig. 2 Scanning electron microscopy on Al–CeO_2 sample after holding at 950 °C for 20 minutes. (A) Secondary electron image showing large grains of Ce_3Al_{11} (bright phase) in an Al matrix (dark). (B) High-magnification backscatter-electron image reveals small Al_2O_3 crystals (red arrows) embedded between Ce_3Al_{11} and Al phases, as well as unreacted oxides. (C)–(E) EDS elemental maps of Al, O, and Ce distribution in the microstructure.

monitor the formation and decomposition of crystalline phases by means of the peak areas of selected peaks (details in ESI†). At selected times, the relative phase fractions were determined by full pattern Rietveld refinement of the diffraction data (insets to Fig. 3).

As soon as melting of aluminum was complete, a rapid conversion of CeO_{2-x} (CaF_2 structure, $Fm\bar{3}m$, lattice parameter a(300 K) = 5.4280(2) Å) to the defect oxide Ce_3O_{5+x} (Bixbyite structure, space group $Ia\bar{3}$, a(1123 K) ≈ 11.37 Å) was observed at all temperatures.[27] At 850 °C (Fig. 3A), Ce_3O_{5+x} reacted then slowly to form the sesquioxide Ce_2O_3 (HT-La_2O_3 structure, $Pm\bar{3}$, a(1123 K) ≈ 3.94 Å, c(1123 K) ≈ 6.17 Å). After 20 min of reaction time, a molar ratio of Ce_3O_{5+x} to Ce_2O_3, normalized by cerium content (*i.e.* $CeO_{1.67+0.5x}$ to $CeO_{1.5}$), of about 1 : 1.7 was determined by Rietveld refinement (inset to Fig. 3A, Table S4, ESI†). Upon cooling of the reaction mixture, the signal for both phases, Ce_3O_{5+x} and Ce_2O_3, disappeared and together with the solidification of the excess aluminum, the crystallization of Ce_3Al_{11} and formation of CeO_{2-x} was observed, in line with observations after DSC.

The reactions were strongly accelerated at 950 °C (Fig. 3B) as the melting of aluminum initiated the rapid conversion of CeO_{2-x} to Ce_3O_{5+x} which then decomposed rapidly to form Ce_2O_3.

Almost instantly, the ternary oxide $CeAlO_3$ ($CaTiO_3$ structure, $Pm\bar{3}m$, a(1223 K) ≈ 3.82 Å) formed and the evolution of relative phase amounts suggests that $CeAlO_3$ was formed by consumption of Ce_2O_3. After 10 min, a ratio of Ce_2O_3 to $CeAlO_3$, normalized by cerium content (*i.e.* $CeO_{1.5}$ to $CeAlO_3$), of about 1 : 93 was observed (Inset to Fig. 3B, Table S4, ESI†). Upon cooling of the reaction mixture, the residual Ce_2O_3 signal dropped to zero, while $CeAlO_3$ remained constant, and Al and Ce_3Al_{11} crystallized from the melt. The experiment at 900 °C (Fig. S7, ESI†), showed essentially a similar order of reactions as at 950 °C. After melting of Al and conversion of CeO_{2-x} to Ce_3O_{5+x}, the latter phase reacted quickly to form Ce_2O_3 and $CeAlO_3$. The relative amount of these phases, however, remained nearly constant over time at a 1 : 10 molar ratio ($CeO_{1.5}$ to $CeAlO_3$). The crystallization of small amounts of Ce_3Al_{11} was observed prior to cooling down from 900 °C.

Thermal effects in DSC appeared delayed compared to the reactions observed in synchrotron data, most likely due to a difference in heating rate and sample mass. The first thermal effect coincides in time with the observed rapid conversion of CeO_{2-x} to Ce_3O_{5+x} and Ce_2O_3 for reactions at 850 °C and 900 °C. Synchrotron data at 900 °C revealed a broad peak in the signal for Ce_2O_3 (Fig. S1, ESI†), suggesting accelerated formation of Ce_2O_3, coinciding with the delayed second signal in the DSC curve. Above 900 °C, the first and second thermal effects seem to overlap in one peak. As the time-resolved synchrotron data indicate the continuous decrease of Ce_2O_3 amount over an extended duration, this suggests that the reduction of Ce_2O_3 to $CeAlO_3$ and subsequently metallic cerium is too slow to show a discernible DSC signal.

The reaction cascade taking place can then be summarized through eqn (2)–(5), omitting non-stoichiometry in the oxides or the dissolution of Ce–Al intermetallic phases in excess $Al_{(l)}$, where the enthalpies were calculated using the thermodynamic database developed for this work. Due to enhanced diffusion in the liquid phase and the strongly negative mixing enthalpy[28] of Ce in $Al_{(l)}$, the excess liquid aluminum present will enrich in Ce content by rapidly dissolving any formed Ce-containing intermetallic compounds. This will remove any formed metallic cerium quickly from the equilibrium reaction, up to the solubility limit (about 7 at% at 900 °C), and precludes the observation of $CeAl_2$ and $CeAl_3$ intermetallic compounds by synchrotron diffraction.

$$CeO_2 + Al \rightarrow \frac{1}{4}Ce_3O_5 + \frac{1}{4}CeAlO_3 - 298\ \text{kJ mol}^{-1} \quad (2)$$

$$Ce_3O_5 + \frac{1}{3}Al \rightarrow \frac{4}{3}Ce_2O_3 + \frac{1}{3}CeAlO_3 - 110\ \text{kJ mol}^{-1} \quad (3)$$

$$Ce_2O_3 + 3Al \rightarrow CeAl_2 + CeAlO_3 - 123\ \text{kJ mol}^{-1} \quad (4)$$

$$CeAlO_3 + 4Al \rightarrow CeAl_3 + Al_2O_3 - 23.8\ \text{kJ mol}^{-1} \quad (5)$$

The sequence of phase formation observed in synchrotron experiments can be rationalized by detailed analysis of the

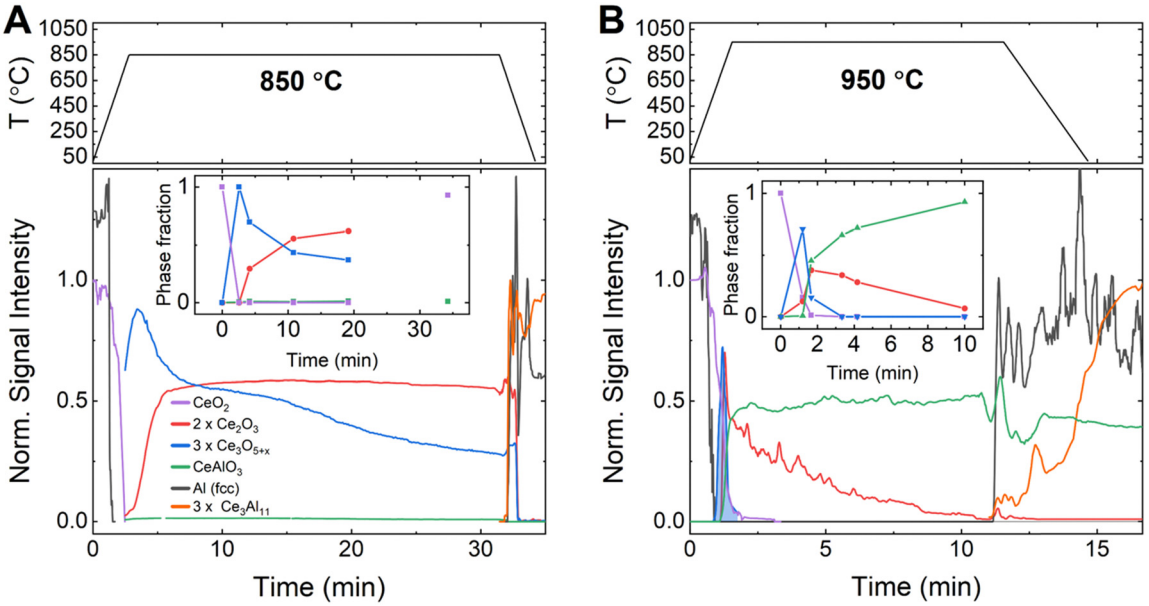

Fig. 3 Phase formation (lower panels) observed by time-resolved synchrotron diffraction for the reaction of Al with CeO_2 at (A) 850 °C and (B) 950 °C, together with temperature programs (upper panels). Curves for respective phases are normalized using results from Rietveld refinements to approximately reflect the evolution of relative phase amounts over time. Insets: Relative amounts of Ce-oxide phases determined at selected times, normalized by Ce content.

computed Al–Ce–O ternary phase diagram (Fig. 4A). The overall compositions (blue cross in Fig. 4A) of the samples are located in the three-phase equilibrium of Ce_3Al_{11} with Al_2O_3 and $(Al,Ce)_{(l)}$, the liquid solution of Ce in Al. The reaction between solid CeO_{2-x} particles and liquid aluminum $Al_{(l)}$ is governed by the formation of product layers at the particle surface and a reaction front that penetrates towards the center of the particles.

As a new phase is formed and expands into the particle from the particle–$Al_{(l)}$ interface, the newly formed phase and excess $Al_{(l)}$ at the particle surface will tend to form the next stable phases in the next local equilibrium. The relative phase amounts observed in a particle over time depend on the competing rates of phase formation (advance of reaction front into particle) and consumption of the phase by the subsequent reaction.

The observed evolution of phase fractions (Fig. 3) deviates significantly from the calculated phase amounts along the Al–CeO_2 vertical section (dashed line in Fig. 4A), which assume immediate and bulk equilibrium conditions (Fig. 4B).

During the first minutes, the rapid conversion of CeO_{2-x} to Ce_3O_{5+x} (eqn (2)) and then Ce_2O_3 (eqn (3)) was observed at all temperatures, in line with the thermodynamic predictions (Fig. 4B). Only the Ce_7O_{12} phase was not observed experimentally, possibly due to the narrow stability window. The fast reactions between CeO_{2-x}, Ce_3O_{5+x} and Ce_2O_3 at all temperatures are in line with the high oxygen diffusion rate and the structural similarity of the cerium oxides.[29–31]

The consequent reaction of Ce_2O_3 with Al to form $CeAlO_3$ (eqn (4)) shows markedly different dynamics depending on temperature, as outlined below. The observed strong temperature dependence of observed phase amounts of Ce_2O_3 and $CeAlO_3$ can be explained by the competition of the diffusion-limited reaction of Ce_2O_3 to $CeAlO_3$ and the consumption of $CeAlO_3$ to form Ce^0 as liquid solution $(Al,Ce)_{(l)}$, and solid $Al_2O_{3(s)}$.

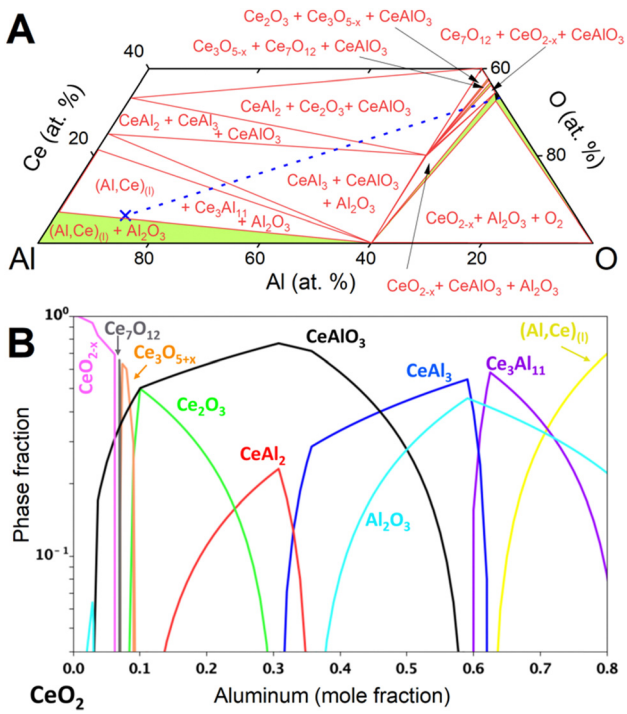

Fig. 4 (A) Calculated isothermal section of the Al–Ce–O system ($x_{Ce} \leq 0.4$) at 950 °C. Two- and three-phase equilibria are given as green and white areas (equilibrium phases indicated), respectively. Narrow two-phase equilibria have been omitted. Composition of synchrotron samples (blue cross) and connecting line (blue, dashed) from CeO_{2-x} to Al are indicated. (B) Phases in equilibrium at 950 °C for compositions along the join from CeO_{2-x} to Al (dashed line in panel A).

At 850 °C, Ce_3O_{5+x} reacts slowly to Ce_2O_3 (eqn (3)) but the consequent conversion to $CeAlO_3$ is extremely slow compared to its reduction to Ce^0 (eqn (5)) and only small quantities of $CeAlO_3$ are therefore observed at any time. The Ce_2O_3 amount remained nearly constant during the observation period.

Rietveld phase fraction analysis of samples after DSC showed that about 63 at% of cerium was reduced to $Ce^0_3Al_{11}$, about 7 at% was found as $Ce^{III}AlO_3$ and 30 at% as unreacted $Ce^{IV}O_2$.

At 900 °C, a steady state between conversion of Ce_2O_3 to $CeAlO_3$ and reduction to Ce^0 is rapidly achieved, although at a much higher ratio of $CeAlO_3$ to Ce_2O_3 than at 850 °C, as diffusion through the product layer is accelerated. About 95 at% of cerium was reduced to $Ce^0_3Al_{11}$, 2 at% was found as $Ce^{III}AlO_3$ and 3% as unreacted CeO_2.

At 950 °C, formation of $CeAlO_3$ from Ce_2O_3 and reduction to Ce^0 progress at similar rates. Ce_2O_3 was mostly consumed over the observation period, but the amount of $CeAlO_3$ had not started to decrease by the time the reaction mixture was cooled down.

In the sample reacted during DSC, about 92 at% of cerium was reduced to $Ce^0_3Al_{11}$ and 8 at% was found as $Ce^{III}AlO_3$.

Equilibrium calculations (Fig. 4) predict reduction of $Ce^{IV}O_{2-x}$ to Ce^0 in the form of compounds $CeAl_2$, $CeAl_3$, Ce_3Al_{11} and finally the liquid solution $(Al,Ce)_{(l)}$. Synchrotron diffraction data showed no evidence of crystalline $CeAl_2$ or $CeAl_3$ and only Ce_3Al_{11} was crystallizing from the liquid solution $(Al,Ce)_{(l)}$. The large excess of $Al_{(l)}$, rapid diffusion in the liquid, and highly negative mixing enthalpy[28] of Ce in $Al_{(l)}$ facilitated rapid removal of cerium from the particle surface into the bulk of the melt.

Conclusions

The results demonstrate the aluminothermic reduction of cerium as a viable, potentially economical, and direct route for the production of Al–Ce alloys, avoiding the costly and energy intensive isolation of cerium metal and providing a high-value use for excess cerium oxide from mine tailings. Material generated in the direct reduction process has a large amount of Al_2O_3 particles embedded in the aluminum matrix expected to contribute to dispersion strengthening in the final alloy. Al–Ce master alloys produced by this process can be used in the Al casting industry after addition of pure Al and other alloying elements (*e.g.* Mg, Si) to tune the desired composition (below 3 at% Ce).[8] The rapid cooling rates observed in typical casting operations can then produce the high-strength eutectic microstructures of Ce_3Al_{11} particles in the Al matrix.

Time-resolved monitoring of the intermediate products revealed a complex multi-step reaction mechanism and clarified the importance of temperature control to maximize reaction yield while minimizing heating costs, which will be crucial for industrial implementation of this process.§

Author contributions

Conceptualization by A. A., D. W., R. T. O, and S. K. M. Methodology, validation by A. A. E. E. M and H. B. H. Investigation and experimentation by A. A., E. E. M, J. S., M. K., S. K., N. H. and A. L. Writing – original draft by A. A. and E. E. M. Writing – review and editing – A. A., E. E. M, H. B. H., J. S., M. K., S. K., N. H., A. L., R. T. O., D. W., and S. K. M. Visualization by A. A.

Conflicts of interest

There are no conflicts to declare.

Acknowledgements

This research was sponsored by the Critical Materials Institute, an Energy Innovation Hub funded by the U.S. Department of Energy (DOE), Office of Energy Efficiency and Renewable Energy and Advanced Manufacturing Office. Work performed at Ames National Laboratory under contract DE-AC02-07CH11358, LLNL under contract DE-AC52-07NA27344. Beamline 12.2.2 at the Advanced Light Source is a DOE Office of Science User Facility under contract no. DE-AC02-05CH11231.

Notes and references

‡ Significant homogeneity ranges were reported for the oxides CeO_{2-x} and Ce_3O_{5+x}.[26,27]

§ Please refer to the ESI† for the Methods section, which includes details of sample preparation, DSC, PXRD, and electron micrograph and spectroscopy data collection, Rietveld refinement, and equilibrium calculations.[32–46]

1 H. C. Örsted, *K. Dan. Vidensk. Selsk.*, 1825.
2 F. Wöhler, *Ann. Phys.*, 1828, **89**, 577–582.
3 A. Holleman, *Band 2 Nebengruppenelemente, Lanthanoide, Actinoide, Transactinoide*, De Gruyter, 2016.
4 F. W. Hall, *Ullmann's Encyclopedia of Industrial Chemistry*, John Wiley & Sons, Ltd, 2000.
5 K. Binnemans, P. T. Jones, K. Van Acker, B. Blanpain, B. Mishra and D. Apelian, *JOM*, 2013, **65**, 846–848.
6 Z. C. Sims, M. S. Kesler, H. B. Henderson, E. Castillo, T. Fishman, D. Weiss, P. Singleton, R. Eggert, S. K. McCall and O. Rios, *J. Sustainable Metall.*, 2022, **8**, 1225–1234.
7 D. J. Cordier, U.S. Geological Survey (2023) Minerals yearbook 2023, can be found under **https://www.usgs.gov/centers/national-minerals-information-center/rare-earths-statistics-and-information**, 2023.
8 Z. C. Sims, O. R. Rios, D. Weiss, P. E. A. Turchi, A. Perron, J. R. I. Lee, T. T. Li, J. A. Hammons, M. Bagge-Hansen, T. M. Willey, K. An, Y. Chen, A. H. King and S. K. McCall, *Mater. Horiz.*, 2017, **4**, 1070–1078.
9 H. B. Henderson, D. Weiss, Z. C. Sims, M. J. Thompson, E. E. Moore, A. Perron, F. Meng, R. T. Ott and O. Rios, in *Light Metals*, ed. A. Tomsett, Springer International Publishing, Cham, 2020, pp. 227–232.
10 R. T. Nguyen, D. D. Imholte, O. R. Rios, D. Weiss, Z. Sims, E. Stromme and S. K. McCall, *Resour., Conserv. Recycl.*, 2019, **144**, 340–349.
11 T. Wu, A. Plotkowski, A. Shyam and D. C. Dunand, *Mater. Sci. Eng.*, 2022, **833**, 142551.

12 L. Chen, J. Yang, Y. Yang, Y. Zhang and Z. Wang, *Mater. Today Commun.*, 2022, **31**, 103714.
13 K. Sheybani, M. H. Paydar and M. H. Shariat, *Int. J. Refract. Met. Hard Mater.*, 2019, **82**, 245–254.
14 K. Sheybani, M. H. Paydar and M. H. Shariat, *Trans. Indian Inst. Met.*, 2020, **73**, 2875–2888.
15 Y. Zhang, X. Hu, F. Liu, J. Yang, L. Chen, W. Tao, A. Liu, Z. Shi and Z. Wang, *J. Alloys Compd.*, 2023, **945**, 169252.
16 J. Yang, M. Kuwabara, Z. Liu, T. Asano and M. Sano, *Tetsu-to-Hagane*, 2006, **92**, 239–245.
17 K. Yoshitaka, J. Yang, Z. Liu and M. Kuwabara, *J. High Temp. Soc.*, 2009, **34**, 20–25.
18 A. Maleki, M. Panjepour, B. Niroumand and M. Meratian, *J. Mater Sci.*, 2010, **45**, 5574–5580.
19 A. Maleki, N. Hosseini and B. Niroumand, *Ceram. Int.*, 2018, **44**, 10–23.
20 J. S. Luna A, A. Flores V, R. Muñiz V, A. F. Fuentes, J. Torres, N. Rodríguez R, J. C. Ortiz and P. Orozco, *J. Rare Earths*, 2011, **29**, 74–76.
21 H. Wang, G. Li, Y. Zhao and G. Chen, *Mater. Sci. Eng.*, 2010, **527**, 2881–2885.
22 S. Vyazovkin, *Isoconversional Kinetics of Thermally Stimulated Processes*, Springer International Publishing, Cham, 2015.
23 H. S. Ray and S. Ray, *Kinetics of Metallurgical Processes*, Springer, Singapore, 2018.
24 H. L. Friedman, *J. Polym. Sci., Part C: Polym. Symp.*, 1964, **6**, 183–195.
25 S. Vyazovkin and C. A. Wight, *Int. Rev. Phys. Chem.*, 1998, **17**, 407–433.
26 D. J. M. Bevan, *J. Inorg. Nucl. Chem.*, 1955, **1**, 49–59.
27 M. Zinkevich, D. Djurovic and F. Aldinger, *Solid State Ionics*, 2006, **177**, 989–1001.
28 M. I. Ivanov, V. V. Berezutskii, M. A. Shevchenko, V. G. Kudin and V. S. Sudavtsova, *Powder Metall. Met. Ceram.*, 2015, **54**, 80–92.
29 S. Ackermann, J. R. Scheffe and A. Steinfeld, *J. Phys. Chem. C*, 2014, **118**, 5216–5225.
30 N. V. Skorodumova, S. I. Simak, B. I. Lundqvist, I. A. Abrikosov and B. Johansson, *Phys. Rev. Lett.*, 2002, **89**, 166601.
31 H. Charlton, G. Baldinozzi and M. Patel, *Front. Nucl. Eng.*, 2023, **1**, 1096142.
32 M. Kunz, A. A. MacDowell, W. A. Caldwell, D. Cambie, R. S. Celestre, E. E. Domning, R. M. Duarte, A. E. Gleason, J. M. Glossinger, N. Kelez, D. W. Plate, T. Yu, J. M. Zaug, H. A. Padmore, R. Jeanloz, A. P. Alivisatos and S. M. Clark, *J. Synchrotron Radiat.*, 2005, **12**, 650–658.
33 A. Doran, L. Schlicker, C. M. Beavers, S. Bhat, M. F. Bekheet and A. Gurlo, *Rev. Sci. Instrum.*, 2017, **88**, 013903.
34 L. Schlicker, A. Doran, P. Schneppmüller, A. Gili, M. Czasny, S. Penner and A. Gurlo, *Rev. Sci. Instrum.*, 2018, **89**, 033904.
35 M. Basham, J. Filik, M. T. Wharmby, P. C. Y. Chang, B. El Kassaby, M. Gerring, J. Aishima, K. Levik, B. C. A. Pulford, I. Sikharulidze, D. Sneddon, M. Webber, S. S. Dhesi, F. Maccherozzi, O. Svensson, S. Brockhauser, G. Náray and A. W. Ashton, *J. Synchrotron Radiat.*, 2015, **22**, 853–858.
36 J. Filik, A. W. Ashton, P. C. Y. Chang, P. A. Chater, S. J. Day, M. Drakopoulos, M. W. Gerring, M. L. Hart, O. V. Magdysyuk, S. Michalik, A. Smith, C. C. Tang, N. J. Terrill, M. T. Wharmby and H. Wilhelm, *J. Appl. Cryst.*, 2017, **50**, 959–966.
37 B. H. Toby and R. B. Von Dreele, *J. Appl. Cryst.*, 2013, **46**, 544–549.
38 L. Kaufman and H. Bernstein, *Computer Calculation of Phase Diagrams With Special Reference to Refractory Metals*, Academic Press Inc., United States, 1970.
39 N. Saunders and A. P. Miodownik, *CALPHAD (Calculation of Phase Diagrams): A Comprehensive Guide*, Elsevier, 1998.
40 H. Lukas, S. G. Fries and B. Sundman, *Computational Thermodynamics: The Calphad Method*, Cambridge University Press, Cambridge, 2007.
41 M. C. Gao, N. Ünlü, G. J. Shiflet, M. Mihalkovic and M. Widom, *Metall. Mater. Trans. A*, 2005, **36**, 3269–3279.
42 H. Mao, M. Selleby and O. Fabrichnaya, *Calphad*, 2008, **32**, 399–412.
43 C. Guéneau, N. Dupin, L. Kjellqvist, E. Geiger, M. Kurata, S. Gossé, E. Corcoran, A. Quaini, R. Hania, A. L. Smith, M. H. A. Piro, T. Besmann, P. E. A. Turchi, J. C. Dumas, M. J. Welland, T. Ogata, B. O. Lee, J. R. Kennedy, C. Adkins, M. Bankhead and D. Costa, *Calphad*, 2021, **72**, 102212.
44 W. T. Fu and D. J. W. Ijdo, *J. Solid State Chem.*, 2006, **179**, 2732–2738.
45 G. Grimvall, *Thermophysical Properties of Materials*, North-Holland, 1986.
46 O. Kubaschewski, *Materials Thermochemistry*, Pergamon Press, New York, 1993.